

# Forecasting the performance of the Minimally Informed foreground cleaning method for CMB polarization observations

Clément Leloup<sup>1,2,\*</sup>, Magdy Morshed<sup>3,4,5</sup>, and Arianna Rizzieri<sup>6</sup>

<sup>1</sup> *Kavli Institute for the Physics and Mathematics of the Universe (WPI), The University of Tokyo Institutes for Advanced Study, The University of Tokyo, Kashiwa, Chiba 277-8583, Japan*

<sup>2</sup> *Center for Data-Driven Discovery, Kavli IPMU (WPI), UTIAS, The University of Tokyo, Kashiwa, Chiba 277-8583, Japan*

<sup>3</sup> *Université Paris-Cité, CNRS, Astroparticule et Cosmologie, F-75013 Paris, France*

<sup>4</sup> *CNRS-UCB International Research Laboratory, Centre Pierre Binétruy, IRL2007, CPB-IN2P3, Berkeley, US*

<sup>5</sup> *INFN Sezione di Ferrara, Via Saragat 1, 44122 Ferrara, Italy and*

<sup>6</sup> *Department of Physics, University of Oxford, Denys Wilkinson Building, Keble Road, Oxford OX1 3RH, United Kingdom*

Astrophysical foreground subtraction is crucial to retrieve the cosmic microwave background (CMB) polarization out of the observed data. Recent efforts [1, 2] have been carried out towards the development of a minimally informed component separation method to handle *a priori* unknown foreground spectral energy distributions (SEDs), while being able to estimate both cosmological, foreground, and potentially instrumental parameters, jointly.

In this paper, we develop a semi-analytical performance forecasting framework for the minimally informed method and we validate it by comparing its results against direct sampling of the harmonic-based likelihood and the pixel domain implementation `MICMAC`. We then use the forecasting tool to demonstrate the robustness of the bias correction procedure introduced in the minimally informed approach. We find that a data-driven approach based on the currently available observational data is enough to efficiently regularize the bias of the method.

## I. INTRODUCTION

The observation of the  $B$ -mode polarization of the Cosmic Microwave Background (CMB) is one of the most important and promising probes for the next stage of cosmological observations. Measuring the amplitude of  $B$  modes at large-scale sourced by gravitational waves produced in the early Universe would be a far-reaching discovery that would open an observational window on the popular and successful theoretical paradigm of cosmic inflation. This would constitute the first direct empirical evidence of the fundamentally quantum nature of gravity by accessing energy scales far higher than those accessible from any other probe. As such, the measurement of CMB  $B$  modes is the primary scientific goal of current (e.g. BICEP [3], Simons Array [4], Simons Observatory [5]) and planned future CMB experiments (e.g. LiteBIRD [6], CMB-S4 [7]).

The challenges faced by these experiments in order to retrieve a robust and precise measurement of the large-scale CMB  $B$  modes are on par with their cosmological significance. They have to address instrumental difficulties since the cosmological signal is expected to be very faint [8], as well as intricate data analysis predicaments, many of which originate from the presence of Galactic foreground emissions at CMB frequencies that are orders of magnitude brighter than the predicted primordial  $B$  modes [9].

Polarized Galactic foregrounds are dominated by synchrotron emissions of charged particles and thermal emissions of dust grain in the interstellar medium, whose exact characteristics are yet to be precisely determined, the best current constraints at CMB frequencies being from Planck observations [10]. Because the evolution of foreground emissions with frequency, their Spectral Energy Distributions (SEDs), is known with limited accuracy, multiple models of the Galactic foregrounds spectra with various levels of complexity are still compatible with the available data [11]. Furthermore, there is now solid evidence that the foreground SEDs are not homogeneous and vary across the sky [12–14]. Until accurate physically motivated foreground emission models are available, it is of primary importance to have access to robust statistical methods of foreground cleaning, a process also known as component separation, that are flexible enough to produce robust cosmological results in the widest range possible of realistic sky models.

As a contribution to addressing this challenge, a new method of foreground cleaning, referred to hereafter as the Minimally Informed (MI) component separation, was developed in [1] with a simple implementation in spherical harmonics domain, later extended to pixel space with the `MICMAC` package described in [2]. However, studying the performance of the MI approach in various contexts to assess its robustness by running these implementations on a large number of sky and/or instrument simulations is very resource intensive. As the MI approach is formulated in the extensively studied statistical principle of maximum likelihood, its performance can be evaluated using simple well-known analytical approximations, in

---

\* clement.leloup@ipmu.jp

the spirit of the two-step framework in [15] based on the parametric component separation method of [16]. This would grant a better understanding of the behavior of the method itself as well as a mean of study, a better control over its assumptions and a way to explore its interaction with instrumental systematic effects [17–21].

This paper describes such a semi-analytical performance forecasting framework for the study of the MI method in the context of multi-frequency CMB polarization experiments. The general formalism of the forecasting approach is described in Section II and an example of case study is presented in Section III where the performance of the MI method is explored as the characteristics of its regularization scheme change for the search of CMB large-scale  $B$  modes with typical ground and space experiments. Finally, the general results of this forecast study are validated using the MICMAC pixel implementation on a small selection of sky simulations, and further discussed in Section IV.

## II. GENERAL FORMALISM

### A. Minimally Informed Component Separation

#### 1. Data model

We suppose the observed data can be summarized in a (frequency  $\nu$ )  $\times$  (pixel  $p$ ) data vector  $\mathbf{d}$  that is a frequency dependent linear combination of  $n_c$  component templates  $\mathbf{s}$  and random noise  $\mathbf{n}$ ,

$$\mathbf{d} = \mathbf{B}\mathbf{s} + \mathbf{n}, \quad (1)$$

where we introduced the mixing matrix  $\mathbf{B}$  whose elements  $B_c^\nu$  is the coefficients of the component  $c$  in the linear combination at frequency  $\nu$ . Following [1], we identify the CMB component  $\mathbf{s}_c = \mathbf{E}\mathbf{s}$ , where  $\mathbf{E}$  is an operator that selects only the CMB component, by imposing the elements of the CMB column of  $\mathbf{B}$  to be fixed to 1 (in CMB units) as well as a Gaussian prior on  $s_c$ . In the absence of further assumptions, the definition of the foreground components is ambiguous as the observed data is invariant under the transformation

$$\mathbf{B} \rightarrow \mathbf{B}' = \mathbf{B} \left[ \begin{array}{c|c} 1 & \mathbf{0}_{n_c-1}^T \\ \hline \mathbf{0}_{n_c-1} & \mathbf{B}_f \end{array} \right]^{-1} \equiv \mathbf{B}\mathbf{M}^{-1}, \quad (2)$$

$$\mathbf{s} \rightarrow \mathbf{s}' = \mathbf{M}\mathbf{s}. \quad (3)$$

In the above expression, we defined  $\mathbf{0}_n$  to be a vector of size  $n$  filled with zeros. To lift this degeneracy, we fix some of the remaining free elements of  $\mathbf{B}$  and take it to

be of the form

$$\mathbf{B} = \left[ \begin{array}{c|c} & \mathbf{b}_f^T \\ \hline \mathbf{B}_c & \mathbb{1}_{n_c-1} \\ \hline & \mathbf{B}_f \end{array} \right], \quad (4)$$

where we have defined the CMB part of the mixing matrix  $\mathbf{B}_c$ , the identity matrix of size  $n \times n$ ,  $\mathbb{1}_n$ , and where  $\mathbf{b}_f$  and  $\mathbf{B}_f$  are a vector and a rectangular matrix of free parameters respectively. This means that each foreground component in the MI approach is not identified from their physical characteristics, but is instead defined as the non-CMB contribution in a selected frequency channel.

#### 2. The likelihood

The extraction of CMB from the foreground contaminated frequency maps is performed in this method by using a maximum likelihood approach. The likelihood is obtained by first assuming that the noise  $\mathbf{n}$  is a multivariate Gaussian with covariance matrix  $\mathbf{N}$  and, as explained in the previous section, that we have a Gaussian prior on the CMB signal component with covariance matrix  $\mathbf{C}$ ,

$$\begin{aligned} \mathcal{S}(\mathbf{s}, \beta, \gamma) &\equiv -2 \ln \mathcal{L} \\ &= \text{const} + (\mathbf{d} - \mathbf{B}(\beta)\mathbf{s})^T \mathbf{N}^{-1} (\mathbf{d} - \mathbf{B}(\beta)\mathbf{s}) \\ &\quad + \mathbf{s}_c^T (\mathbf{C}(\gamma))^{-1} \mathbf{s}_c + \ln |\mathbf{C}(\gamma)|, \end{aligned} \quad (5)$$

where  $|\cdot|$  stands for the determinant, and  $\beta$  and  $\gamma$  are the free parameters of the mixing matrix and CMB covariance respectively. As the constant terms have no impact on the results, we stop including them in the following. We can get rid of the dependence on the signal components  $\mathbf{s}$  and  $\mathbf{s}_c$  by maximizing first over the foreground components, then marginalizing over the CMB component to obtain the spectral likelihood

$$\begin{aligned} \mathcal{S}_{\text{spec}}(\beta, \gamma) &= \mathbf{d}^T \mathbf{P} \mathbf{d} + \hat{\mathbf{s}}_c^T (\mathbf{C} + \hat{\mathbf{N}}_c)^{-1} \hat{\mathbf{s}}_c \\ &\quad + \ln |\mathbf{C} + \hat{\mathbf{N}}_c| - \ln |\hat{\mathbf{N}}_c|. \end{aligned} \quad (6)$$

In the expression of the spectral likelihood above, we introduced the projection operator  $\mathbf{P}$  on the space orthogonal to the columns of  $\mathbf{B}$ , the estimated CMB signal component  $\hat{\mathbf{s}}_c$  and the noise after component separation  $\hat{\mathbf{N}}_c$ , defined respectively by

$$\mathbf{P} \equiv \mathbf{N}^{-1} - \mathbf{N}^{-1} \mathbf{B} (\mathbf{B}^T \mathbf{N}^{-1} \mathbf{B})^{-1} \mathbf{B}^T \mathbf{N}^{-1}, \quad (7)$$

$$\hat{\mathbf{N}}_c \equiv \mathbf{E}^T (\mathbf{B}^T \mathbf{N}^{-1} \mathbf{B})^{-1} \mathbf{E}, \quad (8)$$

$$\hat{\mathbf{s}}_c \equiv \mathbf{E}^T (\mathbf{B}^T \mathbf{N}^{-1} \mathbf{B})^{-1} \mathbf{B}^T \mathbf{N}^{-1} \mathbf{d} \equiv \mathbf{W} \mathbf{d}. \quad (9)$$

In the last equality above, we introduced the weighting operator  $\mathbf{W}$  that linearly combines the frequency dependent observed data to produce the CMB estimated signal  $\hat{\mathbf{s}}_{\mathbf{c}}$ .

It has, however, been shown in [1] that the likelihood (6) is plagued by a significant bias and need to be regularized. In the present work, we consider a different bias correction scheme than the one used in [1], that was initially proposed in [2] and which consists in introducing an ad-hoc correction to the likelihood that now reads

$$\mathcal{S}_{\text{MI}} = \mathbf{d}^T \mathbf{P} \mathbf{d} + \hat{\mathbf{s}}_{\mathbf{c}}^T \left( \mathbf{C} + \hat{\mathbf{N}}_{\mathbf{c}} \right)^{-1} \hat{\mathbf{s}}_{\mathbf{c}} + \ln \left| \mathbf{C} + \hat{\mathbf{N}}_{\mathbf{c}} \right| - \ln \left| \tilde{\mathbf{C}} + \hat{\mathbf{N}}_{\mathbf{c}} \right|, \quad (10)$$

where  $\tilde{\mathbf{C}}$  is a fixed estimate of the CMB covariance matrix. The main goal of the present work is to study the impact of this estimate on the ability to reconstruct the foreground and CMB parameters.

## B. Averaged formalism

We are mostly interested in two quantities: the bias on the cosmological parameters that enter the parameterization of  $\mathbf{C}$  and their standard deviation that give the related statistical errors. As generating and running the component separation over multiple a large number of noise and CMB simulations would be too resource demanding, we adopt a simplified approximate approach following a Fisher-like formalism based on the ensemble averaged likelihood that enables us to reconstruct these two quantities. The component separation formulation as a problem of likelihood maximization allows us to take the noise and CMB average analytically from the likelihood expression. This is easily done by noting that the likelihood (10) can be rephrased in such a way that the data enters the only as a quadratic contribution  $\mathbf{d} \mathbf{d}^T$ , which means that the noise and CMB average of the likelihood only depends on its variance:

$$\left\langle \mathbf{d} \mathbf{d}^T \right\rangle = \left\langle (\mathbf{B} \mathbf{s} + \mathbf{n}) (\mathbf{B} \mathbf{s} + \mathbf{n})^T \right\rangle \equiv \mathbf{D} + \mathbf{N}, \quad (11)$$

where brackets indicate taking the ensemble average over noise and CMB realizations. To get the second equality, we assumed no correlation between the noise  $\mathbf{n}$  and the astrophysical signal  $\mathbf{s}$  which is a weak assumption, and we introduced the variance of the noiseless data  $\mathbf{D}$ . In

simple cases when the data model actually matches the observed sky, it is expressed from the foreground map templates, the true mixing matrix  $\hat{\mathbf{B}}$  and the true CMB covariance  $\hat{\mathbf{C}}$  by:

$$\mathbf{D} = \hat{\mathbf{B}} \left[ \begin{array}{c|c} \hat{\mathbf{C}} & \mathbf{0}_{n_{\mathbf{c}}-1}^T \\ \hline \mathbf{0}_{n_{\mathbf{c}}-1} & \mathbf{s}_{\mathbf{f}} \mathbf{s}_{\mathbf{f}}^T \end{array} \right] \hat{\mathbf{B}}^T. \quad (12)$$

However, keeping it general as  $\mathbf{D}$  allows for the study of cases where there is a mismatch between these as can happen in the presence of systematic effects unaccounted for, for instance.

From this data covariance, we find a simple expression for the noise and CMB averaged likelihood of the MI method,

$$\langle \mathcal{S}_{\text{MI}} \rangle = \text{Tr} \left[ \mathbf{P} \mathbf{D} - \left( \mathbf{C} + \hat{\mathbf{N}}_{\mathbf{c}} \right)^{-1} \hat{\Delta} \right] + \ln \left| \mathbf{C} + \hat{\mathbf{N}}_{\mathbf{c}} \right| - \ln \left| \tilde{\mathbf{C}} + \hat{\mathbf{N}}_{\mathbf{c}} \right|, \quad (13)$$

with the quantity  $\hat{\Delta}$  being the difference between the parameterized CMB covariance and the true covariance in the reconstructed CMB map after component separation,

$$\hat{\Delta} \equiv \mathbf{C} - \mathbf{W} \mathbf{D} \mathbf{W}^T. \quad (14)$$

If the data model matches the actual observed sky and if all the parameters of the likelihood are at their true value, i.e.  $\mathbf{B} = \hat{\mathbf{B}}$  and  $\mathbf{C} = \hat{\mathbf{C}}$ ,  $\hat{\Delta}$  vanishes. Because the cosmological parameters directly enter the parameterization of  $\mathbf{C}$  and, hence, of the likelihood, the bias is simply found as the difference between their value at the peak of the likelihood and their true values,

$$\delta \gamma = \left( \arg \max_{\theta} \langle \mathcal{L}_{\text{MI}} \rangle \right)_{\gamma} - \gamma_{\text{true}}, \quad (15)$$

where  $\theta$  is the concatenated vector of all the free parameters  $\theta = (\beta, \gamma)$ . In our approach, the value at the peak is obtained by finding the parameters that make the gradient of the likelihood vanish. This is enough in the case we considered as the likelihood (13) is sufficiently well-behaved, i.e. there is no saddle point. Therefore, this requires to compute the first derivatives of the averaged likelihood with respect to all the free parameters that enter the likelihood. They are given by,

$$\left\langle \frac{\partial \mathcal{S}_{\text{MI}}}{\partial \beta} \right\rangle = \text{Tr} \left[ \left( \mathbf{C} + \hat{\mathbf{N}}_{\mathbf{c}} \right)^{-1} \hat{\mathbf{N}}_{\mathbf{c},\beta} \left( \mathbf{C} + \hat{\mathbf{N}}_{\mathbf{c}} \right)^{-1} \hat{\Delta} - 2 \mathbf{N}^{-1} \mathbf{B} \left( \mathbf{B}^T \mathbf{N}^{-1} \mathbf{B} \right)^{-1} \mathbf{B}_{,\beta}^T \mathbf{P} \mathbf{D} - \left( \mathbf{C} + \hat{\mathbf{N}}_{\mathbf{c}} \right)^{-1} \hat{\Delta}_{,\beta} + \left( \mathbf{C} + \hat{\mathbf{N}}_{\mathbf{c}} \right)^{-1} \hat{\mathbf{N}}_{\mathbf{c},\beta} - \left( \tilde{\mathbf{C}} + \hat{\mathbf{N}}_{\mathbf{c}} \right)^{-1} \hat{\mathbf{N}}_{\mathbf{c},\beta} \right], \quad (16)$$

$$\left\langle \frac{\partial \mathcal{S}_{\text{MI}}}{\partial \gamma} \right\rangle = \text{Tr} \left[ \left( \mathbf{C} + \hat{\mathbf{N}}_{\mathbf{c}} \right)^{-1} \mathbf{C}_{,\gamma} \left( \mathbf{C} + \hat{\mathbf{N}}_{\mathbf{c}} \right)^{-1} \hat{\Delta} \right]. \quad (17)$$

In the above expressions and in the following, a comma subscript means we are taking the derivative of the operator with respect to the subsequent parameter.

In order to get an estimate of the statistical errors of the parameter once the maximum of the likelihood is found, we assume that the averaged likelihood is Gaussian around its peak. In this case, the covariance matrix between the free parameters is given by the Hessian of the negative averaged log-likelihood,  $-\langle \ln \mathcal{L} \rangle$ , evaluated at its peak. Although not evaluated at the true value of the parameters, it will be referred to in the following as the Fisher information matrix  $\mathcal{F}$ . The estimate of the statistical error is defined from the inverse of the Fisher

matrix following

$$\sigma_\gamma = \sqrt{(\mathcal{F}^{-1})_{\gamma\gamma}}. \quad (18)$$

We know that the full likelihood can not be Gaussian as the derivative of the averaged likelihood with respect to the parameters of  $\mathbf{C}$  (Eq. (17)) vanishes when the parameters are at their true value while the derivatives with respect to the mixing matrix elements (Eq. (16)) is non-zero, which would be impossible for a Gaussian likelihood. However, as we will see in Section III, the likelihood is sufficiently close to Gaussian in the cases under study. Thus, we need the analytical expressions of the second derivatives of the noise and CMB averaged likelihood which are,

$$\begin{aligned} \left\langle \frac{\partial^2 \mathcal{S}_{\text{MI}}}{\partial \beta' \partial \beta} \right\rangle = & \text{Tr} \left[ 2 \left\{ \mathbf{N}^{-1} \mathbf{B} (\mathbf{B}^T \mathbf{N}^{-1} \mathbf{B})^{-1} \mathbf{B}_{,\beta}^T \mathbf{N}^{-1} \mathbf{B} (\mathbf{B}^T \mathbf{N}^{-1} \mathbf{B})^{-1} \mathbf{B}_{,\beta'}^T \mathbf{P} \right. \right. \\ & + \mathbf{N}^{-1} \mathbf{B} (\mathbf{B}^T \mathbf{N}^{-1} \mathbf{B})^{-1} \mathbf{B}_{,\beta'}^T \mathbf{N}^{-1} \mathbf{B} (\mathbf{B}^T \mathbf{N}^{-1} \mathbf{B})^{-1} \mathbf{B}_{,\beta}^T \mathbf{P} - \mathbf{P} \mathbf{B}_{,\beta'} (\mathbf{B}^T \mathbf{N}^{-1} \mathbf{B})^{-1} \mathbf{B}_{,\beta}^T \mathbf{P} \\ & \left. \left. + \mathbf{N}^{-1} \mathbf{B} (\mathbf{B}^T \mathbf{N}^{-1} \mathbf{B})^{-1} \mathbf{B}_{,\beta}^T \mathbf{P} \mathbf{B}_{,\beta'} (\mathbf{B}^T \mathbf{N}^{-1} \mathbf{B})^{-1} \mathbf{B}^T \mathbf{P} - \mathbf{N}^{-1} \mathbf{B} (\mathbf{B}^T \mathbf{N}^{-1} \mathbf{B})^{-1} \mathbf{B}_{,\beta\beta'}^T \mathbf{P} \right\} \mathbf{D} \right. \\ & - 2 \left( \mathbf{C} + \hat{\mathbf{N}}_{\mathbf{c}} \right)^{-1} \hat{\mathbf{N}}_{\mathbf{c},\beta'} \left( \mathbf{C} + \hat{\mathbf{N}}_{\mathbf{c}} \right)^{-1} \hat{\mathbf{N}}_{\mathbf{c},\beta} \left( \mathbf{C} + \hat{\mathbf{N}}_{\mathbf{c}} \right)^{-1} \hat{\Delta} + \left( \mathbf{C} + \hat{\mathbf{N}}_{\mathbf{c}} \right)^{-1} \hat{\mathbf{N}}_{\mathbf{c},\beta\beta'} \left( \mathbf{C} + \hat{\mathbf{N}}_{\mathbf{c}} \right)^{-1} \hat{\Delta} \\ & + \left( \mathbf{C} + \hat{\mathbf{N}}_{\mathbf{c}} \right)^{-1} \hat{\mathbf{N}}_{\mathbf{c},\beta} \left( \mathbf{C} + \hat{\mathbf{N}}_{\mathbf{c}} \right)^{-1} \hat{\Delta}_{,\beta'} + \left( \mathbf{C} + \hat{\mathbf{N}}_{\mathbf{c}} \right)^{-1} \hat{\mathbf{N}}_{\mathbf{c},\beta'} \left( \mathbf{C} + \hat{\mathbf{N}}_{\mathbf{c}} \right)^{-1} \hat{\Delta}_{,\beta} - \left( \mathbf{C} + \hat{\mathbf{N}}_{\mathbf{c}} \right)^{-1} \hat{\Delta}_{,\beta\beta'} \\ & + \left( \mathbf{C} + \hat{\mathbf{N}}_{\mathbf{c}} \right)^{-1} \hat{\mathbf{N}}_{\mathbf{c},\beta\beta'} - \left( \mathbf{C} + \hat{\mathbf{N}}_{\mathbf{c}} \right)^{-1} \hat{\mathbf{N}}_{\mathbf{c},\beta'} \left( \mathbf{C} + \hat{\mathbf{N}}_{\mathbf{c}} \right)^{-1} \hat{\mathbf{N}}_{\mathbf{c},\beta} \\ & \left. - \left( \tilde{\mathbf{C}} + \hat{\mathbf{N}}_{\mathbf{c}} \right)^{-1} \hat{\mathbf{N}}_{\mathbf{c},\beta\beta'} + \left( \tilde{\mathbf{C}} + \hat{\mathbf{N}}_{\mathbf{c}} \right)^{-1} \hat{\mathbf{N}}_{\mathbf{c},\beta'} \left( \tilde{\mathbf{C}} + \hat{\mathbf{N}}_{\mathbf{c}} \right)^{-1} \hat{\mathbf{N}}_{\mathbf{c},\beta} \right], \quad (19) \end{aligned}$$

$$\left\langle \frac{\partial^2 \mathcal{S}_{\text{MI}}}{\partial \beta \partial \gamma} \right\rangle = 2 \text{Tr} \left[ \left( \mathbf{C} + \hat{\mathbf{N}}_{\mathbf{c}} \right)^{-1} \mathbf{C}_{,\gamma} \left( \mathbf{C} + \hat{\mathbf{N}}_{\mathbf{c}} \right)^{-1} \left( \hat{\Delta}_{,\beta} - \hat{\Delta} \left( \mathbf{C} + \hat{\mathbf{N}}_{\mathbf{c}} \right)^{-1} \hat{\mathbf{N}}_{\mathbf{c},\beta} \right) \right], \quad (20)$$

$$\begin{aligned} \left\langle \frac{\partial^2 \mathcal{S}_{\text{MI}}}{\partial \gamma^2} \right\rangle = & \text{Tr} \left[ \left( \mathbf{C} + \hat{\mathbf{N}}_{\mathbf{c}} \right)^{-1} \left( \mathbf{C}_{,\gamma\gamma} - 2 \mathbf{C}_{,\gamma} \left( \mathbf{C} + \hat{\mathbf{N}}_{\mathbf{c}} \right)^{-1} \mathbf{C}_{,\gamma} \right) \left( \mathbf{C} + \hat{\mathbf{N}}_{\mathbf{c}} \right)^{-1} \hat{\Delta} \right. \\ & \left. + \left( \mathbf{C} + \hat{\mathbf{N}}_{\mathbf{c}} \right)^{-1} \mathbf{C}_{,\gamma} \left( \mathbf{C} + \hat{\mathbf{N}}_{\mathbf{c}} \right)^{-1} \mathbf{C}_{,\gamma} \right]. \quad (21) \end{aligned}$$

From our parameterization of the mixing matrix using its elements directly, the second derivatives of  $\mathbf{B}$  all vanish. The expression of the first and second derivatives of  $\hat{\mathbf{N}}_{\mathbf{c}}$  and  $\hat{\Delta}$  with respect to  $\beta$  are given in Appendix A. We summarize the procedure that allows us to estimate the bias  $\delta\gamma$  and statistical errors  $\sigma_\gamma$  for the cosmological parameters  $\gamma$ :

1. We define the noiseless data covariance operator  $\mathbf{D}$  from simulations of the observed sky as implicitly defined in Eq. (11).
2. We explore the parameter space of the likelihood to find its maximum as the position where all of the derivatives of Eq. (16)-(17) vanish and recover the bias  $\delta\gamma$  as the distance between their value at the

peak of the likelihood and their true values, as in Eq. (15).

3. We compute the Fisher information matrix  $\mathbf{F}$  that corresponds to the Hessian of the negative averaged log-likelihood at the likelihood maximum found in step 2. from Eq. (19)-(20). The estimate of the statistical error  $\sigma_\gamma$  is found from its inverse using Eq. (18).
4. Results from the two previous steps are then used to run extensive tests in order to extract general results on the performance of the method. These are eventually validated by running the MICMAC package on a small set of selected simulations.

The analysis pipeline described above and used in Section III is illustrated in FIG. 1.

Although this procedure is very simple and builds on analytical expressions, the matrix algebra is only tractable when working in harmonic space which requires foregrounds with spatially homogeneous scaling as well as homogeneous noise. This is a strong limitation of the framework which is therefore not able to give quantitative results regarding the performance of the method to complex foregrounds. However, it is well suited to study its robustness to effects that can be decoupled from the complexity of the foregrounds such as systematic effects as is still done with various other component separation methods, see e.g. [17–21]. In addition, it is also not impossible that the approach followed in [22] to analytically estimate the foreground leakage when using a spatially variable component separation from the homogeneous case could be adapted to the present approach and give a quantitative estimate of  $\delta r$  and  $\sigma_r$  even when dealing with spatially varying foregrounds. In the meantime, the general results derived from the framework presented here will be further validated by running the pixel version implemented in the MICMAC package on specific noise and CMB realizations.

As an application of the procedure, and an interesting study in itself, we will use this formalism in the next section to explore the robustness of the minimally informed component separation to change in its correction term  $\tilde{\mathbf{C}}$ .

### III. DEPENDENCE ON THE CORRECTION TERM

#### A. Implementation of the formalism

We present here the specific implementation of the formalism presented in Section II. As previously mentioned, the approach needs to be used in the harmonic domain in order to be tractable in a short time. Working in the harmonic domain is also convenient as the covariance of the CMB signal is best expressed as its angular power-spectrum. As most future CMB experiments will focus on the measurement of its polarization, i.e.  $Q$  and  $U$  Stokes parameters of the pixelized micro-wave sky which correspond to  $E$  and  $B$  modes in the harmonic domain, we will focus on these and will not consider the CMB intensity  $I$ . For simplicity and because there is no conclusive evidence that the  $Q$  and  $U$  SEDs are different, we use the same mixing matrix for both  $E$  and  $B$  modes. The CMB  $E$  and  $B$ -mode signal covariance in harmonic space is their angular power-spectrum, which we evaluate at multipoles up to  $\ell < \ell_{\max} = 256$  and with minimum multipole constrained by the sky coverage of the experimental set-ups.

Because the main scientific goal of upcoming CMB experiments is the measurement of large-scale  $B$  modes, where the cosmological signal relevant for cosmic inflation is to be found, only the CMB primordial  $B$  mode

power-spectrum will be fitted for, the contributions in the  $E$  modes and the lensing part of the  $B$  modes will be assumed to be purely Gaussian and perfectly known. The impact of an imperfect knowledge of these, of non-Gaussianities of the lensing  $B$ -modes as well as the capabilities of the methodology to recover them is left for future work. The theoretical spectra are obtained with CAMB [23] using the cosmological parameters from the Planck 2018 cosmological analysis best-fit [24]. The multipole-dependent CMB  $B$ -mode signal covariance used in the likelihood (13) is parameterized as

$$(\mathbf{C}^{BB})_{\ell}(r) = C_{\ell}^{BB}(r) = rC_{\ell}^{BB,\text{prim}} + C_{\ell}^{BB,\text{lens}}. \quad (22)$$

Ground experiment						
$\nu$ (GHz)	27	39	93	145	225	280
Sensitivity ( $\mu\text{K-arcmin}$ )	49.5	29.7	3.7	4.7	8.9	22.6
$f_{\text{sky}}$	$\sim 10\%$					

TABLE I. Principal characteristics of the ground experiment set-up used in this study: center frequency of the frequency bands, sensitivity in polarization and observed fraction of the sky.

Here  $C_{\ell}^{BB,\text{prim}}$  is the primordial contribution to  $B$  modes,  $C_{\ell}^{BB,\text{lens}}$  is the contribution from gravitationally lensed  $E$  modes computed with the CAMB code [25] using Planck parameters [24], and  $r$  is the tensor-to-scalar ratio which is assumed to be the only free parameter of the CMB covariance for this study, whose bias and statistical error constitute our main figures of merit. Following the assumptions in [1] and [2], we use the lensing power-spectrum  $C_{\ell}^{BB,\text{lens}}$  as our baseline for the estimated CMB  $B$ -mode covariance  $(\tilde{\mathbf{C}}^{BB})_{\ell}$  and study how the performance of the method changes around this baseline. As it would not make sense to explore the impact of varying the estimated CMB  $E$ -mode covariance  $\tilde{\mathbf{C}}^{EE}$  without adjusting for it, we assume  $(\tilde{\mathbf{C}}^{EE})_{\ell}$  to be the theoretical  $E$ -mode power-spectrum used to produce the CMB simulated data.

Similarly to the CMB covariance, the noise covariance is given by its angular power spectrum  $\mathbf{N}_{\ell}$ , and we assume a frequency-channel dependent white noise in the following. The level of this white noise is determined by the experimental set-up under consideration. The specific set-ups we consider correspond to a ground based experiment, with characteristics based on the SO-SATS [26] that we detail in TABLE I, and a space-borne experiment with properties based on LiteBIRD [27] detailed in TABLE II.

The fraction of the sky observable by the experiment determines the lowest multipole accessible from the ob-

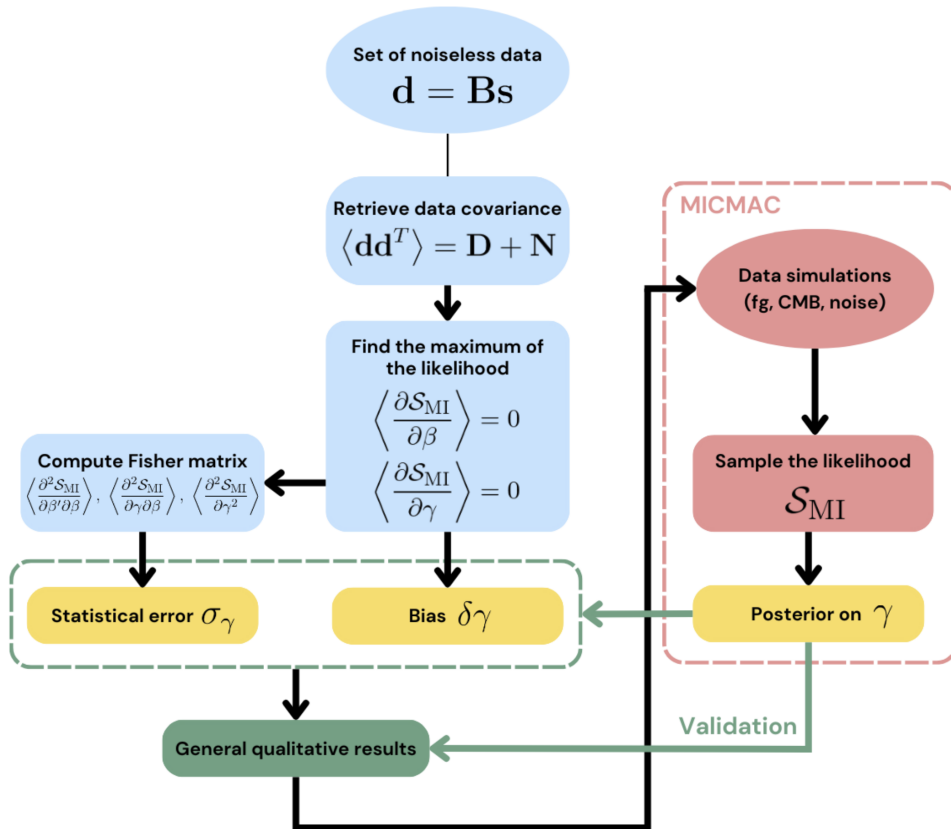


FIG. 1. Schematic view of the different steps of a typical analysis involving the use of the simplified Fisher forecast approach developed in Section II, including the validation of the results using the MICMAC package which directly samples the likelihood in Eq. (10). It is, in particular, used in the study of the correction term presented in Section III.

served data. In the following we will be using multipoles in the range  $30 \leq \ell \leq 256$  for the Ground experiment, and  $2 \leq \ell \leq 256$  for the Space experiment. In addition, the fraction of the sky observed will affect the statistical uncertainties on the parameters as less degrees of freedom are accessible to observation. This reduction of power is taken into account by including an overall global factor of  $f_{\text{sky}}$  in the likelihood (13), that appears from the unobserved  $m$  multipoles at a given  $\ell$ . This allows us to stay in the domain of spherical harmonics coefficient and to avoid any  $E$ -to- $B$  leakage that would arise from an overly simplistic masking procedure. This approximation only affects the statistical uncertainties and not the bias that appears as a local value of  $\gamma$  in the observed patch of the sky, but this induced bias should vanish when averaging over CMB and noise realizations. Thus, the results using the averaged likelihood should not be affected. It has been verified by comparing with the pixel implementation in MICMAC [2] which properly takes the effect of the mask into account, that the approximation described here gives consistent results.

From the current knowledge of the polarized foregrounds in the frequency range under consideration, see

e.g. [10], we assume the presence of two polarized foreground components, therefore assuming a three-column mixing matrix. The foreground templates with their spatially homogeneous SED are taken from the `d0` model for Galactic thermal dust and the `s0` model for synchrotron emission of the PySM software [29, 30]. This choice is motivated by our implementation in the space of spherical harmonic coefficients which is not suited to handle more complex foregrounds with spatial variations of their SEDs. The true CMB covariance  $\hat{\mathbf{C}}$  used in the definition of the data covariance  $\mathbf{D}$  is taken to have the same form as Eq. (22) with values of the tensor-to-scalar ratio  $r$  specified for each case.

## B. Validation of the forecasting tool

We start our study by validating the accuracy of the forecasting approach described in Section II. This validation is performed by comparing its results with those obtained from the direct sampling of the averaged likelihood (13) with the Monte-Carlo Markov Chain (MCMC) package `emcee` [32], for a range of cases from small to

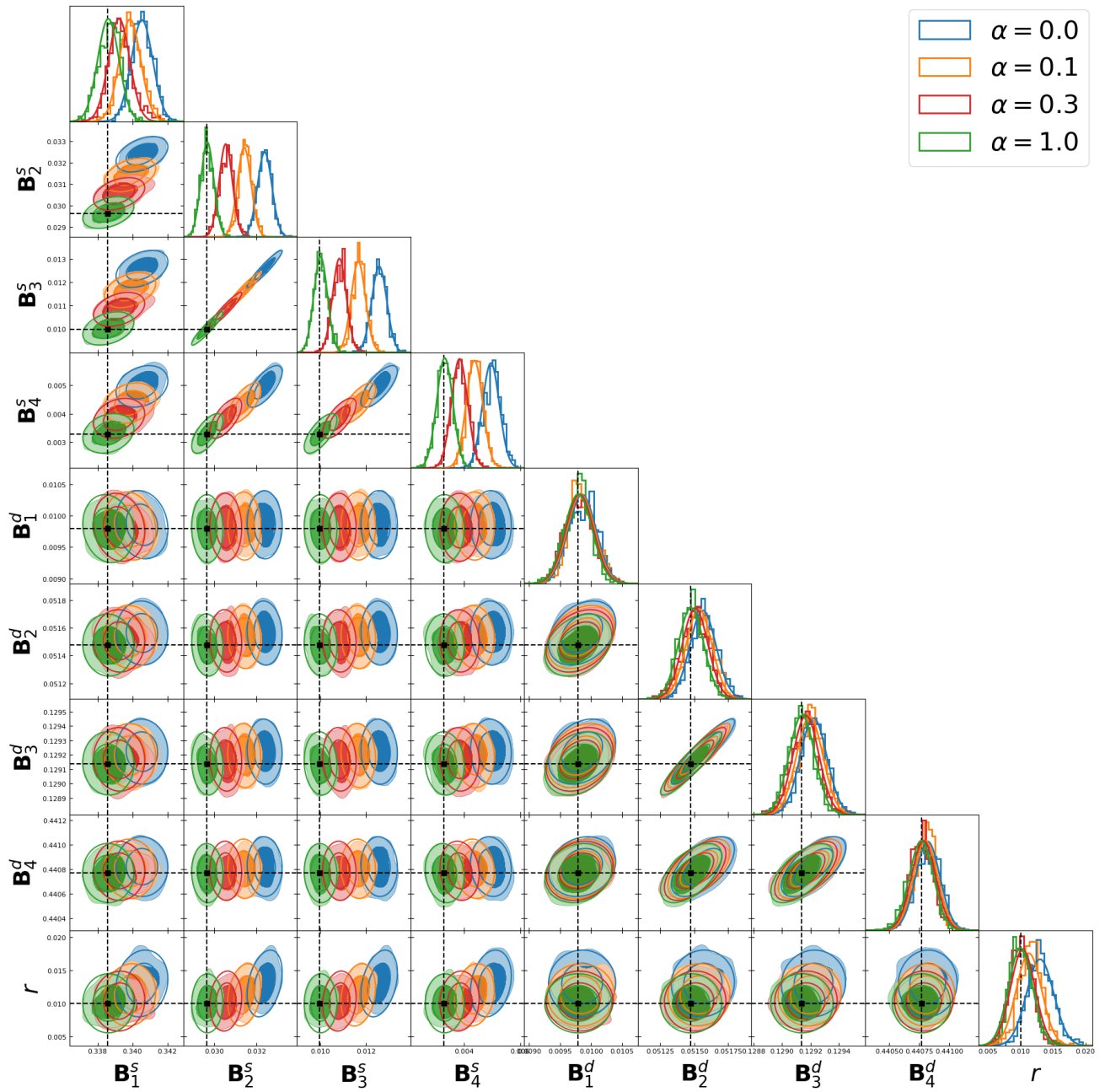


FIG. 2. 2D and 1D densities for the free parameters of the likelihoods in Eq. (13), i.e. the free elements of the mixing matrix  $\mathbf{B}$  and the tensor-to-scalar ratio  $r$ , for the ground experiment case and for various values of the amplitude  $\alpha$  of the CMB covariance estimate (see Eq. (23)). The 2D filled contours are obtained by directly sampling the likelihood (13) including  $\sim 1000$  independent samples for each case and are plotted using the `GetDist` package [31], while the ellipses are calculated from the bias and Fisher information matrix defined in our simplified formalism. Similarly, the 1D histograms are from the sampling while the Gaussian curves are from the simplified formalism. The mixing matrix elements are displayed in the format  $\mathbf{B}_\nu^c$ , where  $\nu \in 0 \dots 5$  are the frequency channels and  $c \in s, d$  correspond to the foreground component ( $s$  for synchrotron and  $d$  for dust). The black points and dashed lines correspond to the true value of the parameters used to produce the input signal. In all cases, the model of foregrounds used is `d0s0`.

large bias on  $r$ . To produce a large variety of cases, we introduce a degree of freedom in the correction parameter of the averaged likelihood by varying the amplitude

of the CMB  $B$ -mode covariance estimate,

$$\left(\tilde{\mathbf{C}}^{BB}(\alpha)\right)_\ell = \alpha \cdot C_\ell^{BB,\text{lens}}, \quad (23)$$

Space-borne experiment			
$\nu$ (GHz)	Sensitivity ( $\mu\text{K-arcmin}$ )	$\nu$ (GHz)	Sensitivity ( $\mu\text{K-arcmin}$ )
40	37.42	140	4.79
50	33.46	166	5.57
60	21.31	195	5.85
68	16.87	235	10.79
78	12.07	280	13.80
89	11.3	337	21.95
100	6.56	402	47.45
119	4.58		
$f_{\text{sky}}$	$\sim 50\%$		

TABLE II. Characteristics of the space-borne experiment set-up used in this study: center frequency of the frequency bands, sensitivity in polarization and observed fraction of the sky. Although a space-borne experiment has access to the entirety of the sky, we use the Planck HFI mask [28] to hide the Galactic plane, leaving an effective sky fraction of approximately half of the sky.

as it was shown in [1] that when  $\alpha = 0$ , the bias on  $r$  is significant, while in the case  $\alpha = 1$  it is negligible with respect to the statistical uncertainty. Results with various values of  $\alpha$  are shown in FIG. 2 in the context of the ground experiment set-up. This comparison shows that the simplified Fisher approach is a really good approximation of the averaged likelihood and is able to quantitatively recover not only the bias, but also the covariance of the varying parameters.

From these results, we conclude that the formalism developed in Section II is a useful tool that can be used for our study of robustness of the method to the correction term, and that the noise and CMB averaged likelihood is approximately Gaussian near its peak for small and large biases which allow us to focus on the bias  $\delta r$  and Fisher error  $\sigma_r$ .

### C. Exploration of the correction term's impact

#### 1. CMB estimate amplitude

Based on the implementation presented in Section III A, we can further study how the performance of the MI method behaves, in terms of  $\delta r$  and  $\sigma_r$ , as the CMB estimate  $\tilde{\mathbf{C}}$  entering the correction term changes. We start by studying the performance of the method in both the ground based and space-borne experimental set-

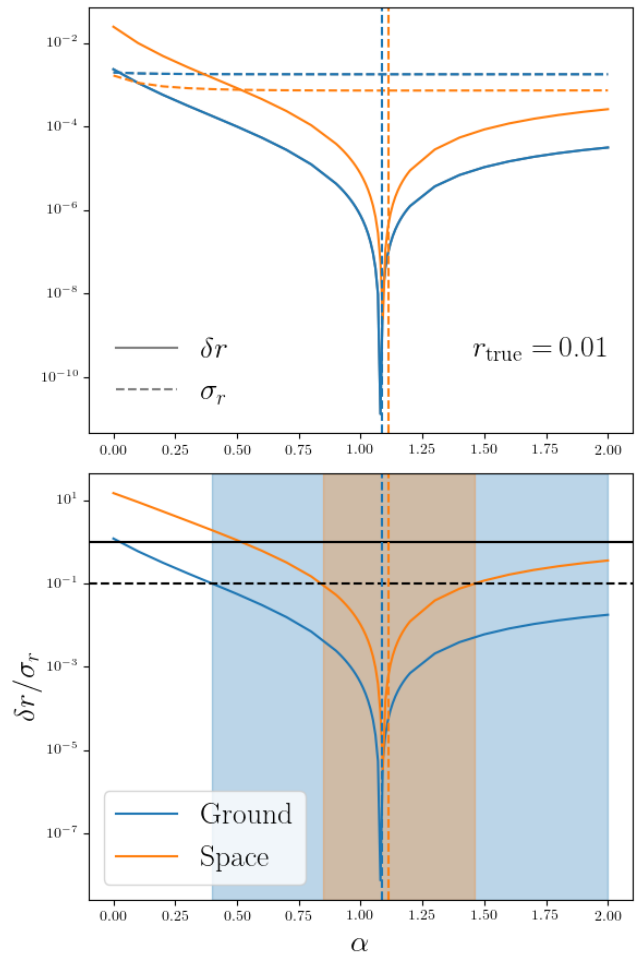


FIG. 3. Forecast of the MI approach robustness to a varying amplitude  $\alpha$  of the correction term defined in Eq. (23), in terms of  $\delta r$ ,  $\sigma_r$  (Top) and their ratio (Bottom) calculated using the simplified Fisher forecast approximation described in Section II for both the ground-based and space-borne instrumental configurations. The shaded areas correspond to the interval of  $\alpha$  for which  $\delta r \leq 0.1\sigma_r$ , and the vertical dashed lines to the estimation of  $\alpha_{\text{min}}$  from Eq. (26). The solid and dashed horizontal lines correspond to  $\delta r/\sigma_r = 1$  and  $0.1$  respectively. In this figure, the true value of the tensor-to-scalar ratio is assumed to be  $r_{\text{true}} = 0.01$ . Results exhibit the same qualitative behavior for the other values tested,  $r_{\text{true}} = 0.0$  and  $0.001$ .

ups while varying the amplitude of  $\tilde{\mathbf{C}}$ , following the parameterization given in Eq. (23). Results are found in FIG. 3 for a value of  $r_{\text{true}} = 0.01$ .

We see that for the bias to be small as compared to the standard deviation, using the 10% threshold as an indicator, the correction needs not be too close to the lensing power-spectrum, especially for our ground based experimental set-up. The satellite experiment can tolerate a range of  $\alpha \in [0.85, 1.46]$ , so with a width of  $\sim 0.6$ , while the ground experiment can withstand a range of  $\alpha$  from  $\sim 0.4$  all the way to the upper limit of our interval



of exploration  $\alpha = 2$ . The wider range for the latter compared to the former is driven by the fact that the bias is larger in general, and to a lesser extent because the sensitivity is better for the space-borne set-up. This is due to the larger  $\ell$  range accessible from space, given that we use the same  $\ell_{\max}$ , and to the higher-dimensionality of the parameter space since there are many more frequency channels. For  $r_{\text{true}} = 0.001$  or 0, the range is similar in width for both the ground and the space-borne experiment.

An interesting fact that we can see here is that the actual minimum of the bias is not for  $\alpha = 1$  where the correction term is obtained by using the exact lensing power spectrum, but for some  $\alpha_{\min} > 1$ . This can be understood by looking at the value of the gradient of the averaged likelihood at the true value of the parameters,  $\mathbf{B} = \hat{\mathbf{B}}$  and  $\mathbf{C} = \hat{\mathbf{C}}$ ,

$$\begin{aligned} \left\langle \frac{\partial \mathcal{S}_{\text{MI}}}{\partial \beta} \right\rangle \Big|_{\beta, r = \beta_{\text{true}}, r_{\text{true}}} &= \text{Tr} \left[ \left( \mathbf{C} + \hat{\mathbf{N}}_{\mathbf{c}} \right)^{-1} \hat{\mathbf{N}}_{\mathbf{c}, \beta} \right. \\ &\quad \left. - \left( \tilde{\mathbf{C}} + \hat{\mathbf{N}}_{\mathbf{c}} \right)^{-1} \hat{\mathbf{N}}_{\mathbf{c}, \beta} \right] \\ &= \sum_{\ell, m} \text{Tr} \left[ \left( \left( r_{\text{true}} \mathbf{C}_{\ell}^{\text{prim}} + \mathbf{C}_{\ell}^{\text{lens}} + \hat{\mathbf{N}}_{\mathbf{c}} \right)^{-1} \right. \right. \\ &\quad \left. \left. - \left( \alpha \mathbf{C}_{\ell}^{\text{lens}} + \hat{\mathbf{N}}_{\mathbf{c}} \right)^{-1} \right) \hat{\mathbf{N}}_{\mathbf{c}, \beta} \right], \end{aligned} \quad (24)$$

$$\left\langle \frac{\partial \mathcal{S}_{\text{MI}}}{\partial r} \right\rangle \Big|_{\beta, r = \beta_{\text{true}}, r_{\text{true}}} = 0. \quad (25)$$

Therefore there is an  $\alpha_{\min}(\beta_{\text{true}}, r_{\text{true}})$  that is  $> 1$  for positive values of  $r_{\text{true}}$ , that exactly cancels the right hand side of Eq. (24). In general, this minimum value will be different for each spectral parameter  $\beta$ , except when  $r_{\text{true}} = 0$  for which there is a common trivial solution  $\alpha_{\min} = 1$ . So, for a given  $r_{\text{true}}$  the optimal value will be a compromise  $\alpha_{\min} \geq 1$  that does not completely cancel the bias. However, because  $\hat{\mathbf{N}}_{\mathbf{c}, \beta}$  is independent of  $\ell$  in our case,  $\alpha_{\min}$  is the same for each spectral parameter, and the bias is exactly canceled. Of course, because it depends on the true values of the parameters, this optimal value of  $\alpha$  that minimizes the bias is not known in advance. A good and intuitive approximation to find  $\alpha_{\min}$  in the case under study, whose result is included in FIG. 3, is to assume that  $r_{\text{true}} \mathbf{C}_{\ell}^{\text{prim}} + \mathbf{C}_{\ell}^{\text{lens}} + \hat{\mathbf{N}}_{\mathbf{c}}$  is constant with respect to  $\ell$  which is approximately the case past the reionization bump and until the first peak of the lensing spectrum. Under this approximation, the minimum is found at

$$\alpha_{\min} \simeq 1 + r_{\text{true}} \frac{\sum_{\ell} (2\ell + 1) \mathbf{C}_{\ell}^{\text{prim}}}{\sum_{\ell} (2\ell + 1) \mathbf{C}_{\ell}^{\text{lens}}}, \quad (26)$$

where the sum runs over the multipole range accessible to the experiment. This assumption is best fulfilled in the

range of multipoles where  $\mathbf{C}_{\ell}^{\text{lens}} + \hat{\mathbf{N}}_{\mathbf{c}}$  dominates, which makes the above approximation better as the true value of the tensor-to-scalar ratio  $r_{\text{true}}$  is small. It is a particularly good approximation for the Ground experiment even at higher values of  $r_{\text{true}}$  as the largest scales, at which the primordial contribution dominates, are not included in its accessible multipole range.

## 2. Multipole range

Another degree of freedom of the correction term one can play with is the multipole range over which it is applied, in particular the lowest multipole  $\ell_{\min}$  from which the CMB estimate is considered, i.e. such that

$$\left( \tilde{\mathbf{C}}^{BB}(\ell_{\min}) \right)_{\ell} = \begin{cases} 0 & \text{if } \ell \leq \ell_{\min} \\ \mathbf{C}_{\ell}^{BB, \text{lens}} & \text{otherwise} \end{cases} \quad (27)$$

The decision to study this parameter is motivated by the fact that the primordial part of the  $B$ -mode power-spectrum is dominant at low multipoles, while it is small compared to the lensing power-spectrum at higher multipoles. Therefore, by canceling the correction term at multipoles below  $\ell_{\min}$ , the range  $\ell \leq \ell_{\min}$  can be understood as the signal region in which the tensor-to-scalar ratio is measured. On the other hand, the range  $\ell \geq \ell_{\min}$  is interpreted as a side-band where the foreground parameters are measured. Although this is an intuitive interpretation, it is also too simplistic as the side-band also brings some contribution to the constraint on  $r$  and the signal region helps measuring foreground parameters.

The performance of the method in terms of  $\delta r$  and  $\sigma_r$  as a function of  $\ell_{\min}$  is shown in FIG. 4 for both experimental set-up and  $r_{\text{true}} = 0.01$ . It appears that there is a range of  $\ell_{\min} > 0$  such that the bias is  $\delta r \leq 0.1\sigma_r$  when  $r_{\text{true}} = 0.01$ , the highest such multipole being 140 and 60 for ground and space experiments respectively. This limit multipole is rather stable as the true value of the tensor-to-scalar ratio decreases, with limits at 147 and 66 when  $r_{\text{true}} = 0.001$ , and 148 and 64 when  $r_{\text{true}} = 0$ .

We see that the performance of the method decreases as  $\ell_{\min}$  increases which is easily understood since as  $\ell_{\min}$  grows, the contribution of more and more multipoles is not corrected.

## 3. From available data

From the previous results obtained in this section, it appears that there is some tolerance to the correction term in order to make the inherent bias from the method small as compared to the statistical error. A legitimate approach to try, based on this general result, is whether the  $B$ -mode data currently available is enough to produce a model-independent estimate of the CMB covariance  $\tilde{\mathbf{C}}$  that can be used in the correction term and can guarantee

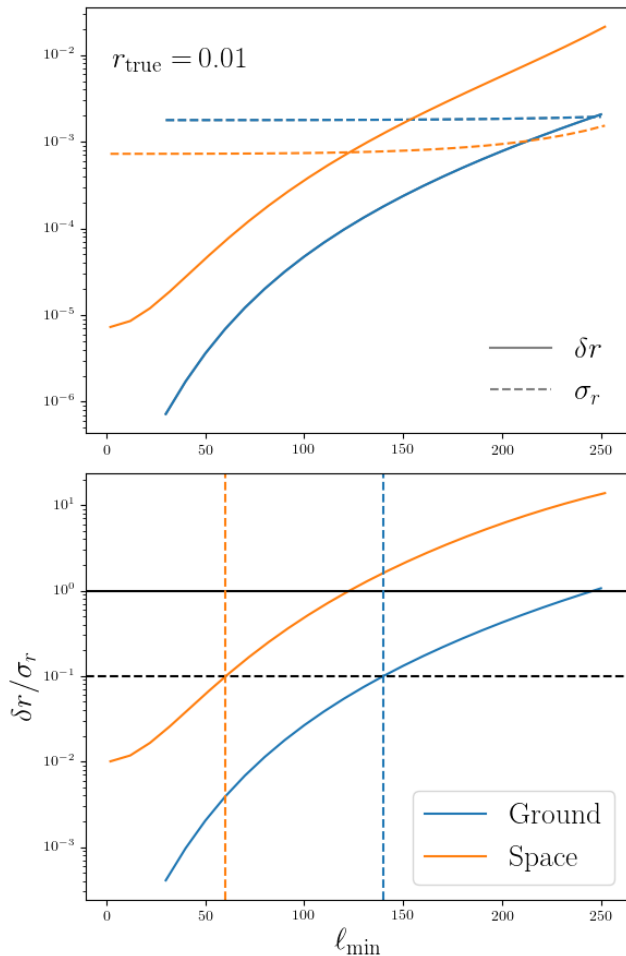


FIG. 4. Forecast of the MI approach robustness to a varying lowest multipole  $\ell_{\min}$  of the correction term defined in Eq. (27), in terms of  $\delta r$ ,  $\sigma_r$  (Top) and their ratio (Bottom) calculated using the simplified Fisher forecast approximation described in Section II for both the ground-based and space-borne instrumental configurations. The vertical dashed lines correspond to the maximum multipole  $\ell_{\min}$  such that  $\delta r \leq 0.1\sigma_r$ , which are at  $\ell_{\min} = 134$  and  $\ell_{\min} = 71$  for ground and space experiments respectively. The solid and dashed horizontal lines correspond to  $\delta r/\sigma_r = 1$  and  $0.1$  respectively. In this figure, the true value of the tensor-to-scalar ratio is assumed to be  $r_{\text{true}} = 0.01$ . Results exhibit the same qualitative behavior for the other values tested,  $r_{\text{true}} = 0.0$  and  $0.001$ .

that  $\delta r$  will be small enough that it is not a problem to be worried about.

To explore this approach, we use the measured binned  $B$ -mode power-spectra from three datasets: BICEP/Keck 2018 observation season [3], SPT-Pol [33] and the POLARBEAR 2-year data release [34]. These give tight constraints on the shape of the  $B$ -mode CMB power-spectrum, *a priori* coming from the gravitational lensing of  $E$  modes, over the wide range of multipoles  $37 \leq \ell \leq 2302$ . This interval far extends the multipole

range used in the forecast, however we noticed that the inclusion of each of the three datasets has a noticeable impact, even at low multipoles.

Because we want this estimate to be model-independent, we need a tool to produce a function of  $\ell$  based solely on data points. We therefore choose to use Gaussian Processes as a simple way to achieve this goal. We use the Gaussian Process package of `scikit-learn` [35] with the built-in radial basis function kernel operator to produce the data-based  $\tilde{\mathbf{C}}$  since it can handle data points with error-bars. However, its implementation requires the error-bars to be symmetrical, therefore we simply decided to symmetrize them by taking the maximum of the lower and upper errors from the data. We also neglect the correlations between the data points of single experiments, and correlations between experiments. The CMB power-spectrum estimated from existing datasets is shown in FIG. 5 along with the data points and the theoretical spectra used to produce the CMB part of the noiseless data variance  $\mathbf{D}$ .

We use the developed forecast framework to study the performance of the MI approach when using the mean of the Gaussian process result in place of our estimate of the CMB  $B$ -mode covariance, as a function of the true value of the tensor-to-scalar ratio. As a mean of comparison, we run through the same cases using  $(\tilde{\mathbf{C}}^{BB})_{\ell} = C_{\ell}^{BB, \text{lens}}$ . The results of this comparative evaluation can be found in FIG. 6.

It is reassuring to see that the performance using the Gaussian process is good in general, with  $\delta r < 0.1\sigma_r$  over the whole range of  $r_{\text{true}}$  for the ground experiment and  $\delta r < 0.2\sigma_r$  for the space mission, the largest biases being at low values of  $r_{\text{true}}$ .

The bias is driven by the fact that the  $B$ -mode power-spectrum of the Gaussian process mean has a larger amplitude than the CMB lensing spectrum and vanishes for the lowest multipoles, i.e. a combination of both effects studied previously corresponding to an effective  $\alpha$  slightly larger than 1 and an effective  $\ell_{\min} \simeq 5 - 10$ . The latter effect has no impact on the ground based experimental set-up as its multipole range includes only  $30 \leq \ell$ , while we have seen in FIG. 3 that the former effect has a bigger impact on the space experiment.

#### IV. VALIDATION AND DISCUSSIONS

We have seen in the previous Section how the forecasting simplified approach can be used to study the dependency of the performance as the CMB estimate  $\tilde{\mathbf{C}}$  that enters in the regularization of the likelihood changes. We have found that, taking as criterion  $\delta r \leq 0.1\sigma_r$ , the method can accommodate for a range of amplitude mismatch with the true power-spectrum. The performance is also good when the regularization scheme is not applied to the whole range of multipoles. From these results, we could understand intuitively how using a Gaussian

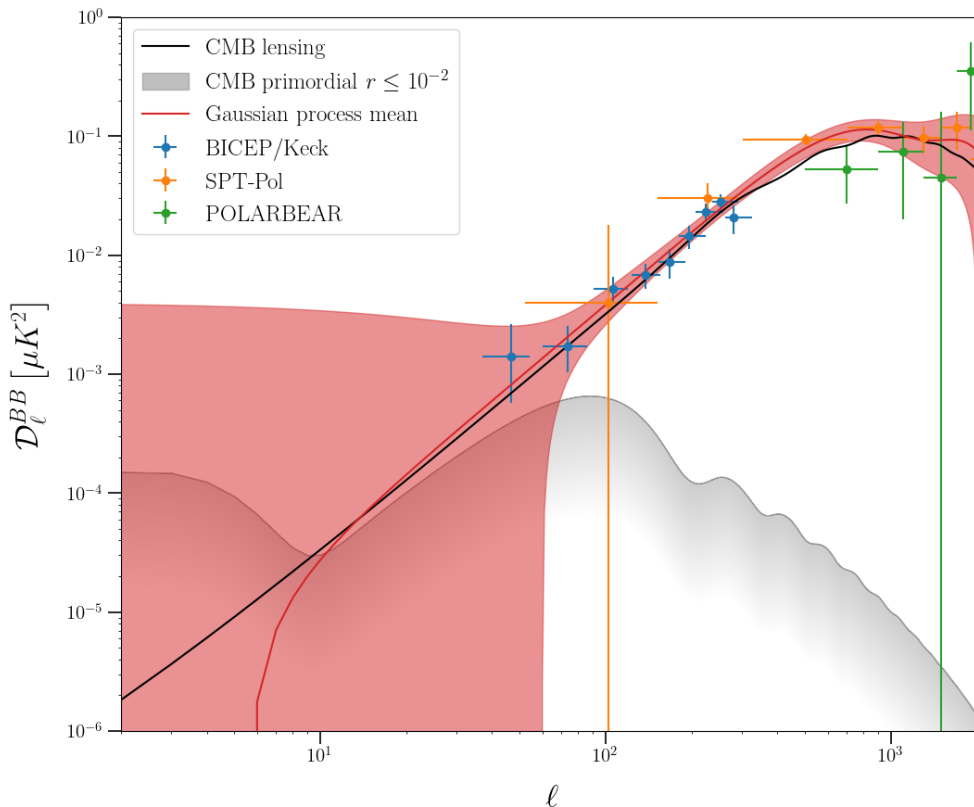


FIG. 5. Theoretical  $B$ -mode power spectra of the CMB lensing and primordial gravitational waves for values of  $r \leq 10^{-2}$  used to produce the noiseless data covariance  $\mathbf{D}$  and used as reference for the CMB estimate  $\tilde{\mathbf{C}}$  of the correction term. The data points are current best measurements from BICEP/Keck [3], SPT-Pol [33] and POLARBEAR [34], with their error bars, used to produce the Gaussian process mean estimate (red solid line) and its  $1\sigma$  confidence interval (shaded red area).

process produced from current observations of CMB  $B$  modes as  $\tilde{\mathbf{C}}$  seemed to be already enough to lead to low bias, for both the ground experiment and space-borne mission.

However, from the limitations of the forecasting approach mentioned at the end of Section II, it is necessary to validate these results using an established implementation likely to be used in actual data analysis, following the pipeline described in FIG. 1. To this end, we explore a small number of configurations corresponding to cases described in Section III on a few simulations of CMB and noise, with the MICMAC [2] package.

### A. Choice of the case study

In order to validate the forecasting approach with MICMAC (right side of the pipeline in FIG. 1), a total of six different configurations for  $\tilde{\mathbf{C}}$  are considered with a space mission configuration and input tensor-to-scalar

ratio value taken to be  $r_{\text{true}} = 0.01$ . To avoid potential issues with the masking procedure, we perform the component separation on the full sky. Given how we account for the sky fraction in the forecasting approach, we expect that this will not affect the bias and will reduce the statistical error by a factor of  $\sqrt{f_{\text{sky}}} \sim 0.7$  as compared to a space mission observing half the sky.

All corresponding runs are performed on HEALPix [36] grid maps featuring a resolution of  $n_{\text{side}} = 128$  and a maximum multipole of  $\ell_{\text{max}} = 256$ .

As the MICMAC package is computationally expensive, a quantitative validation based on the averaging over many different realizations and Gibbs chains is not feasible. The validation methodology adopted is instead based on the repeatability of the sampling steps given different correction procedures, with a more qualitative validation of the forecasting approach.

For each configuration, five sets of input maps are generated as linear mixture of random CMB realizations from the theoretical power spectra, Gaussian noise ob-

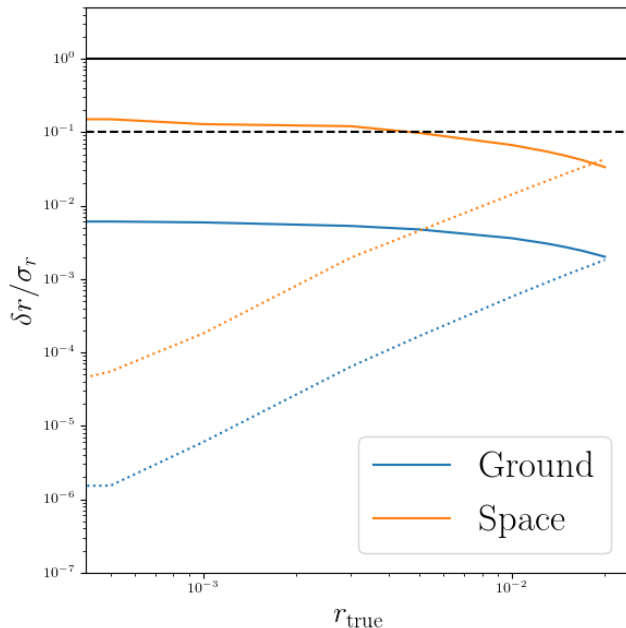


FIG. 6. Forecast of the MI approach robustness as a function of  $r_{\text{true}}$ , in terms of  $\delta r$ ,  $\sigma_r$  (Top) and their ratio (Bottom) calculated using the simplified Fisher forecast approximation described in Section II for both the ground-based and space-borne instrumental configurations. The CMB estimates  $\tilde{\mathbf{C}}$  used in the correction term are the mean of the Gaussian process produced from the datasets described in Section III C 3 (solid) and the CMB lensing power-spectrum itself (dotted). The solid and dashed horizontal lines correspond to  $\delta r/\sigma_r = 1$  and 0.1 respectively.

tained from the space mission noise levels, and d0s0 foreground maps as provided by the PySM software. To each realization is associated a fixed random seed to perform the Gibbs sampling, ensuring that each correction configuration runs with the exact same of parameters over the exact same five set of simulated input frequency maps, differing only by the choice of the CMB estimate  $\tilde{\mathbf{C}}$ .

As previously noted, the input simulated maps are computed as a set of  $Q$  and  $U$  pixel maps, and  $E$  and  $B$  modes are accounted for in the sampling. We follow the same procedure as in the previous sections, fitting for cosmological parameters and varying the correction term only for the  $B$  modes.

The different choices of configurations for  $\tilde{\mathbf{C}}^{BB}$  are:

1. **No correction:** without correction, i.e. taking  $\alpha = 0$  in Eq. (23), as a reference biased case, with a bias predicted by the forecasting approach to be of the order  $\delta_r \sim 10\sigma_r \sim 3 \times 10^{-2}$ . As the implementation in MICMAC can not handle the exact case  $\alpha = 0$  for numerical reasons, we instead take  $\alpha = 10^{-10}$  which should exhibit the same behavior,
2. **Theoretical:** taking the theoretical  $B$ -mode lensing power spectrum computed by CAMB, which is the

$\tilde{\mathbf{C}}^{BB}$  that would be taken for a typical MICMAC run, associated to a prediction of  $\delta_r \sim 10^{-2}\sigma_r \sim 10^{-5}$ ,

3. **Lower correction:** taking the  $BB$  lensing power spectrum computed by CAMB multiplied to  $\alpha = 0.5$  as in Eq. (23) and studied with the forecasting tool in Section III C 1, with a predicted bias  $\delta_r \sim \sigma_r/2 \sim 5 \times 10^{-4}$ ,
4. **No lower modes:** taking the  $BB$  lensing power spectrum computed by CAMB with  $\ell_{\text{min}} = 100$ , as in Section III C 2, predicted to be biased as  $\delta_r \sim \sigma_r/5 \sim 2 \times 10^{-4}$ ,
5. **Gaussian Process:** taking the data-based Gaussian process power spectrum studied in Section III C 3, with  $\delta_r \sim 5 \times 10^{-3}\sigma_r \sim 5 \times 10^{-6}$ .

As in the previous sections, the fixed estimate of the CMB  $E$  modes is taken to be identical as the input CMB power spectrum.

It should be emphasized that the validation procedure relies here on a limited number of realizations, and as such will not be able to recover precisely the lowest  $\delta_r$  biases compared to  $\sigma_r$ . In particular, we expect to retrieve the same order of magnitude and not the exact value of  $\delta_r$  mentioned above.

## B. Results and discussions

The results are summarized in FIG. 7, displaying the different  $r$  posteriors for each of the configuration.

The theoretical  $\tilde{\mathbf{C}}$  and the Gaussian process cases are consistent with the input  $r$  value. Both configurations have very close posteriors, which is expected as their corresponding biases are negligible compared to the statistical error on  $r$  and all configurations depart from the same seed.

The  $\ell_{\text{min}} = 100$  configuration is also compatible with the input  $r$  value, although slightly biased with the five realizations giving  $\delta_r^{\ell_{\text{min}}=100} = 4 \times 10^{-4}$ . This bias is consistent with the expectation of  $\delta_r \sim \sigma_r/5$ .

The configurations parametrized by  $\alpha$  as in Eq. (23) are associated to a greater bias, with  $\delta_r^{\alpha=0.5} = 6 \times 10^{-4}$  and  $\delta_r^{\alpha=10^{-10}} = 2.5 \times 10^{-2}$ , which is consistent with the predictions of  $\delta_r \sim \sigma_r/2$  and  $\delta_r \sim 10\sigma_r$  respectively.

As the three cases  $\ell_{\text{min}} = 100$ ,  $\alpha = 0.5$  and  $\alpha = 10^{-10}$  featuring large biases correspond in fact to quite poor choices of  $\tilde{\mathbf{C}}^{BB}$ , these results highlight a relatively important margin in the choice of  $\tilde{\mathbf{C}}^{BB}$ , and the relevance of a data-driven choice. We mention as well that the ground based experiment is predicted to be much less impacted by a poor choice of  $\tilde{\mathbf{C}}^{BB}$  since the smaller observed sky fraction means that less modes contribute to the bias and the statistical error is increased.

The study of the possible deviation of fixed CMB estimate for the  $E$  modes is left for future studies focused on

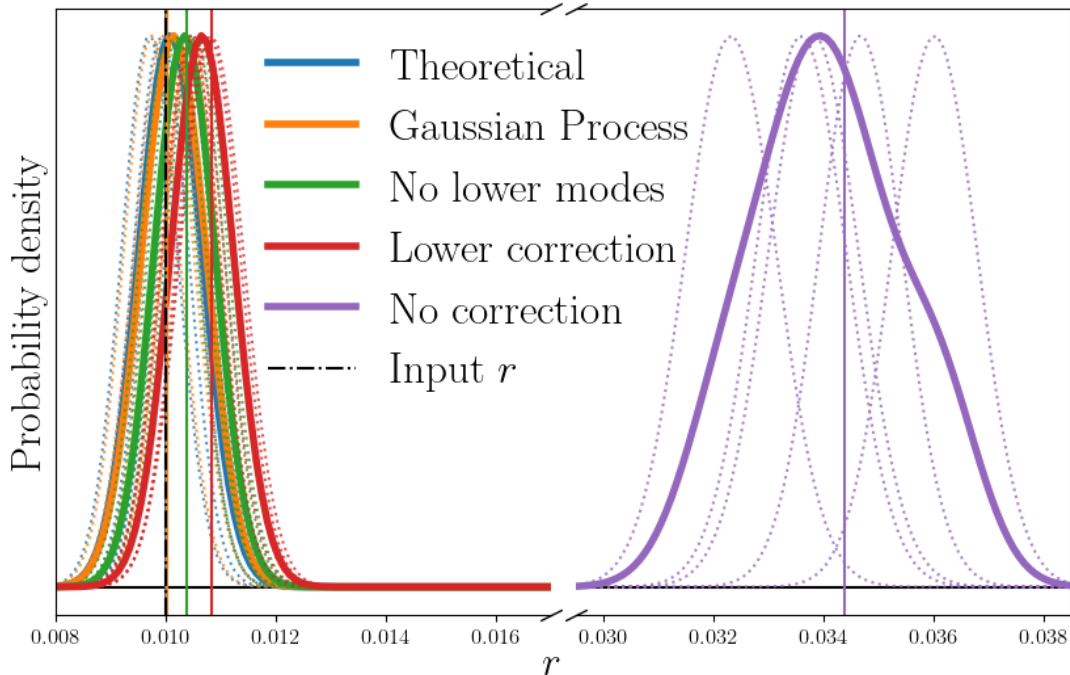


FIG. 7. Probability densities of the  $r$  posterior for each configuration described in Section IV A. For each configuration, the solid bold line is the average of the probability densities represented as thin solid lines of the same color. For clarity, the  $x$ -axis is cut between  $r = 0.017$  and  $r = 0.0295$ . For each configuration, the vertical solid lines denote the corresponding forecast bias predictions. The **Theoretical** and **Gaussian Process** cases biases predictions are very small compared to the statistical error.

the retrieval of  $E$  modes, both in harmonic and pixel domain. While we expect a deviation of  $\tilde{\mathbf{C}}^{EE}$  to impact the retrieved parameters as more signal is not canceled out, we also expect to have a better signal over noise ratio to better characterize the  $E$ -mode power spectrum.

## V. CONCLUSIONS

In the present work, we developed and validated a forecasting approach for the minimally informed component separation method based on the Fisher formalism. This approach is able to quantitatively estimate the bias and statistical error of cosmological parameters for very little computational cost. Although currently limited to foreground models with constant SEDs across the sky, it is expected that this forecasting tool will render possible future impact studies of instrumental systematic effects on the performance of the MI method, as well as to optimize its hyper-parameters and validate its general assumptions.

A general analysis pipeline for such studies has been proposed, capitalizing on both the fast estimation by the forecasting tool and the accurate but more involved evaluation by the full pixel-based package MICMAC. As an illustration, we followed this procedure to study the im-

part of the CMB covariance estimate  $\tilde{\mathbf{C}}$  on the performance of the MI method, and in particular as a regularization for its bias. We were able to find a wide variety of configurations for  $\tilde{\mathbf{C}}$  departing from the theoretical CMB lensing  $B$ -mode covariance and such that the bias is unnoticeable given the statistical error. This builds confidence that the accuracy of  $\tilde{\mathbf{C}}$  necessary for the ad-hoc bias correction procedure will not be a limiting factor when applied to actual observations, strengthening the case for the MI approach.

## ACKNOWLEDGEMENTS

We would like to thank Radek Stompior and Josquin Errard for fruitful discussions and feedback on the draft. The authors acknowledge the use of the HEALPix [36] and healpy packages [37, 38], and the JAX package [39]. This work was granted access to the HPC resources of IDRIS under the allocation 2024-102865 made by GENCI. These resources were allocated to the SCIPOL project [40] funded by the European Research Council (ERC) under the European Union’s Horizon 2020 research and innovation program (PI: Josquin Errard, Grant agreement No. 101044073).

MM is funded by the European Union (ERC, RELiCS, project number 101116027). Views and opinions ex-

pressed are however those of the author(s) only and do not necessarily reflect those of the European Union or the

European Research Council Executive Agency. Neither the European Union nor the granting authority can be held responsible for them.

- 
- [1] C. Leloup, J. Errard, and R. Stompor, Nonparametric maximum likelihood component separation for CMB polarization data, *Phys. Rev. D* **108**, 123547 (2023), arXiv:2308.03412 [astro-ph.CO].
- [2] M. Morshed, A. Rizzieri, C. Leloup, J. Errard, and R. Stompor, Pixel domain implementation of the Minimally Informed CMB MAP foreground Cleaning (MICMAC) method, (2024), arXiv:2405.18365 [astro-ph.CO].
- [3] P. A. R. Ade *et al.* (BICEP, Keck), Improved Constraints on Primordial Gravitational Waves using Planck, WMAP, and BICEP/Keck Observations through the 2018 Observing Season, *Phys. Rev. Lett.* **127**, 151301 (2021), arXiv:2110.00483 [astro-ph.CO].
- [4] A. Suzuki *et al.* (POLARBEAR), The POLARBEAR-2 and the Simons Array Experiment, *J. Low Temp. Phys.* **184**, 805 (2016), arXiv:1512.07299 [astro-ph.IM].
- [5] P. Ade *et al.* (Simons Observatory), The Simons Observatory: Science goals and forecasts, *JCAP* **02**, 056, arXiv:1808.07445 [astro-ph.CO].
- [6] A. Lee *et al.*, LiteBIRD: an all-sky cosmic microwave background probe of inflation, in *Bulletin of the American Astronomical Society*, Vol. 51 (2019) p. 286.
- [7] K. N. Abazajian *et al.* (CMB-S4), CMB-S4 Science Book, First Edition, arXiv e-prints (2016), arXiv:1610.02743 [astro-ph.CO].
- [8] J. Martin, C. Ringeval, and V. Vennin, Encyclopædia Inflationaris, *Phys. Dark Univ.* **5-6**, 75 (2014), arXiv:1303.3787 [astro-ph.CO].
- [9] N. Krachmalnicoff, C. Baccigalupi, J. Aumont, M. Bersanelli, and A. Mennella, Characterization of foreground emission on degree angular scales for CMB B-mode observations - Thermal dust and synchrotron signal from Planck and WMAP data, *Astron. Astrophys.* **588**, A65 (2016), arXiv:1511.00532 [astro-ph.CO].
- [10] Y. Akrami *et al.* (Planck), Planck 2018 results. IV. Diffuse component separation, *Astron. Astrophys.* **641**, A4 (2020), arXiv:1807.06208 [astro-ph.CO].
- [11] The Pan-Experiment Galactic Science Group, <https://galsci.github.io/>, accessed: 2023-07-10.
- [12] R. Adam *et al.* (Planck), Planck 2015 results. X. Diffuse component separation: Foreground maps, *Astron. Astrophys.* **594**, A10 (2016), arXiv:1502.01588 [astro-ph.CO].
- [13] N. Krachmalnicoff *et al.*, S-PASS view of polarized Galactic synchrotron at 2.3 GHz as a contaminant to CMB observations, *Astron. Astrophys.* **618**, A166 (2018), arXiv:1802.01145 [astro-ph.GA].
- [14] V. Pelgrims *et al.*, Evidence for Line-of-Sight Frequency Decorrelation of Polarized Dust Emission in *Planck* Data, *Astron. Astrophys.* **647**, A16 (2021), arXiv:2101.09291 [astro-ph.CO].
- [15] R. Stompor, J. Errard, and D. Poletti, Forecasting performance of CMB experiments in the presence of complex foreground contaminations, *Phys. Rev. D* **94**, 083526 (2016), arXiv:1609.03807 [astro-ph.CO].
- [16] R. Stompor, S. M. Leach, F. Stivoli, and C. Baccigalupi, Maximum Likelihood algorithm for parametric component separation in CMB experiments, *Mon. Not. Roy. Astron. Soc.* **392**, 216 (2009), arXiv:0804.2645 [astro-ph].
- [17] T. Ghigna, T. Matsumura, G. Patanchon, H. Ishino, and M. Hazumi, Requirements for future CMB satellite missions: photometric and band-pass response calibration, *JCAP* **11**, 030, arXiv:2004.11601 [astro-ph.IM].
- [18] C. Vergès, J. Errard, and R. Stompor, Framework for analysis of next generation, polarized CMB data sets in the presence of Galactic foregrounds and systematic effects, *Phys. Rev. D* **103**, 063507 (2021), arXiv:2009.07814 [astro-ph.CO].
- [19] B. Jost, J. Errard, and R. Stompor, Characterizing cosmic birefringence in the presence of Galactic foregrounds and instrumental systematic effects, *Phys. Rev. D* **108**, 082005 (2023), arXiv:2212.08007 [astro-ph.CO].
- [20] M. Monelli, E. Komatsu, T. Ghigna, T. Matsumura, G. Pisano, and R. Takaku, Impact of half-wave plate systematics on the measurement of CMB B-mode polarization, *JCAP* **05**, 018, arXiv:2311.07999 [astro-ph.CO].
- [21] C. Leloup *et al.* (LiteBIRD), Impact of beam far side-lobe knowledge in the presence of foregrounds for LiteBIRD, *JCAP* **06**, 011, arXiv:2312.09001 [astro-ph.CO].
- [22] J. Errard and R. Stompor, Characterizing bias on large scale CMB B-modes after galactic foregrounds cleaning, *Phys. Rev. D* **99**, 043529 (2019), arXiv:1811.00479 [astro-ph.CO].
- [23] A. Lewis, A. Challinor, and A. Lasenby, Efficient computation of CMB anisotropies in closed FRW models, *Astrophys. J.* **538**, 473 (2000), arXiv:astro-ph/9911177 [astro-ph].
- [24] N. Aghanim *et al.* (Planck), Planck 2018 results. VI. Cosmological parameters, *Astron. Astrophys.* **641**, A6 (2020), [Erratum: *Astron. Astrophys.* 652, C4 (2021)], arXiv:1807.06209 [astro-ph.CO].
- [25] C. Howlett, A. Lewis, A. Hall, and A. Challinor, Cmb power spectrum parameter degeneracies in the era of precision cosmology, *Journal of Cosmology and Astroparticle Physics*.
- [26] P. Ade *et al.* (Simons Observatory), The Simons Observatory: Science goals and forecasts, *JCAP* **02**, 056, arXiv:1808.07445 [astro-ph.CO].
- [27] E. Allys *et al.* (LiteBIRD), Probing Cosmic Inflation with the LiteBIRD Cosmic Microwave Background Polarization Survey, *PTEP* **2023**, 042F01 (2023), arXiv:2202.02773 [astro-ph.IM].
- [28] P. Collaboration, The Planck Legacy Archive, <https://pla.esac.esa.int>, accessed: 2024-08-09.
- [29] B. Thorne, J. Dunkley, D. Alonso, and S. Naess, The Python Sky Model: software for simulating the Galactic microwave sky, *Mon. Not. Roy. Astron. Soc.* **469**, 2821 (2017), arXiv:1608.02841 [astro-ph.CO].
- [30] A. Zonca, B. Thorne, N. Krachmalnicoff, and J. Borrill, The Python Sky Model 3 software, *J. Open Source Softw.* **6**, 3783 (2021), arXiv:2108.01444 [astro-ph.IM].
- [31] A. Lewis, GetDist: a Python package for analysing Monte Carlo samples, (2019), arXiv:1910.13970 [astro-

- ph.IM].
- [32] D. Foreman-Mackey, D. W. Hogg, D. Lang, and J. Goodman, emcee: The MCMC Hammer, Publications of the Astronomical Society of the Pacific **125**, 306 (2013), arXiv:1202.3665 [astro-ph.IM].
- [33] J. T. Sayre *et al.* (SPT), Measurements of B-mode Polarization of the Cosmic Microwave Background from 500 Square Degrees of SPTpol Data, Phys. Rev. D **101**, 122003 (2020), arXiv:1910.05748 [astro-ph.CO].
- [34] P. A. R. Ade *et al.* (POLARBEAR), A Measurement of the Cosmic Microwave Background *B*-Mode Polarization Power Spectrum at Sub-Degree Scales from 2 years of POLARBEAR Data, Astrophys. J. **848**, 121 (2017), arXiv:1705.02907 [astro-ph.CO].
- [35] F. Pedregosa *et al.*, Scikit-learn: Machine learning in Python, Journal of Machine Learning Research **12**, 2825 (2011).
- [36] K. M. Gorski, B. D. Wandelt, F. K. Hansen, E. Hivon, and A. J. Banday, The HEALPix Primer, arXiv e-prints , astro-ph/9905275 (1999), arXiv:astro-ph/9905275 [astro-ph].
- [37] A. Zonca, L. Singer, D. Lenz, M. Reinecke, C. Rosset, E. Hivon, and K. Gorski, healpy: equal area pixelization and spherical harmonics transforms for data on the sphere in python, Journal of Open Source Software **4**, 1298 (2019).
- [38] K. M. Górski, E. Hivon, A. J. Banday, B. D. Wandelt, F. K. Hansen, M. Reinecke, and M. Bartelmann, HEALPix: A Framework for High-Resolution Discretization and Fast Analysis of Data Distributed on the Sphere, Astrophysical Journal **622**, 759 (2005), arXiv:astro-ph/0409513.
- [39] J. Bradbury, R. Frostig, P. Hawkins, M. J. Johnson, C. Leary, D. Maclaurin, G. Necula, A. Paszke, J. VanderPlas, S. Wanderman-Milne, and Q. Zhang, JAX: composable transformations of Python+NumPy programs, <http://github.com/google/jax> (2018).
- [40] Scipol website, <https://scipol.in2p3.fr/>.

### Appendix A: Derivatives entering the Fisher information matrix

We describe here the first and second derivatives of the noise after component separation  $\hat{\mathbf{N}}_{\mathbf{c}}$  and of the difference between the estimated and true CMB covariance  $\hat{\mathbf{\Delta}}$  with respect to the foreground parameters  $\beta$  that enter the expression of the Fisher information matrix elements in Eq. (19)-(21):

$$\hat{\mathbf{N}}_{\mathbf{c}} = \mathbf{E}^T (\mathbf{B}^T \mathbf{N}^{-1} \mathbf{B})^{-1} \mathbf{E}, \quad (\text{A1})$$

$$\hat{\mathbf{N}}_{\mathbf{c},\beta} = -\mathbf{E}^T (\mathbf{B}^T \mathbf{N}^{-1} \mathbf{B})^{-1} (\mathbf{B}_{,\beta}^T \mathbf{N}^{-1} \mathbf{B} + \mathbf{B}^T \mathbf{N}^{-1} \mathbf{B}_{,\beta}) (\mathbf{B}^T \mathbf{N}^{-1} \mathbf{B})^{-1} \mathbf{E}, \quad (\text{A2})$$

$$\begin{aligned} \hat{\mathbf{N}}_{\mathbf{c},\beta\beta'} &= 2\mathbf{E}^T (\mathbf{B}^T \mathbf{N}^{-1} \mathbf{B})^{-1} \left[ -\mathbf{B}_{,\beta\beta'}^T \mathbf{N}^{-1} \mathbf{B} + \mathbf{B}^T \mathbf{N}^{-1} \mathbf{B}_{,\beta} (\mathbf{B}^T \mathbf{N}^{-1} \mathbf{B})^{-1} \mathbf{B}_{,\beta'}^T \mathbf{N}^{-1} \mathbf{B} - \mathbf{B}_{,\beta}^T \mathbf{P} \mathbf{B}_{,\beta'} \right. \\ &\quad \left. + \mathbf{B}^T \mathbf{N}^{-1} \mathbf{B}_{,\beta'} (\mathbf{B}^T \mathbf{N}^{-1} \mathbf{B})^{-1} \mathbf{B}^T \mathbf{N}^{-1} \mathbf{B}_{,\beta} + \mathbf{B}^T \mathbf{N}^{-1} \mathbf{B}_{,\beta} (\mathbf{B}^T \mathbf{N}^{-1} \mathbf{B})^{-1} \mathbf{B}^T \mathbf{N}^{-1} \mathbf{B}_{,\beta'} \right] (\mathbf{B}^T \mathbf{N}^{-1} \mathbf{B})^{-1} \mathbf{E}. \quad (\text{A3}) \end{aligned}$$

$$\hat{\mathbf{\Delta}} = \mathbf{C} - \mathbf{E}^T (\mathbf{B}^T \mathbf{N}^{-1} \mathbf{B})^{-1} \mathbf{B}^T \mathbf{N}^{-1} \mathbf{D} \mathbf{N}^{-1} \mathbf{B} (\mathbf{B}^T \mathbf{N}^{-1} \mathbf{B})^{-1} \mathbf{E}, \quad (\text{A4})$$

$$\hat{\mathbf{\Delta}}_{,\beta} = 2\mathbf{E} (\mathbf{B}^T \mathbf{N}^{-1} \mathbf{B})^{-1} \left( \mathbf{B}^T \mathbf{N}^{-1} \mathbf{B}_{,\beta} (\mathbf{B}^T \mathbf{N}^{-1} \mathbf{B})^{-1} \mathbf{B}^T \mathbf{N}^{-1} - \mathbf{B}_{,\beta}^T \mathbf{P} \right) \mathbf{D} \mathbf{N}^{-1} \mathbf{B} (\mathbf{B}^T \mathbf{N}^{-1} \mathbf{B})^{-1} \mathbf{E}, \quad (\text{A5})$$

$$\begin{aligned} \hat{\mathbf{\Delta}}_{,\beta\beta'} &= 2\mathbf{E} (\mathbf{B}^T \mathbf{N}^{-1} \mathbf{B})^{-1} \left[ \left( \mathbf{B}^T \mathbf{N}^{-1} \mathbf{B}_{,\beta\beta'} (\mathbf{B}^T \mathbf{N}^{-1} \mathbf{B})^{-1} \mathbf{B}^T \mathbf{N}^{-1} - \mathbf{B}_{,\beta\beta'}^T \mathbf{P} + \mathbf{B}_{,\beta}^T \mathbf{P} \mathbf{B}_{,\beta'} (\mathbf{B}^T \mathbf{N}^{-1} \mathbf{B})^{-1} \mathbf{B}^T \mathbf{N}^{-1} \right. \right. \\ &\quad \left. \left. + \mathbf{B}_{,\beta'}^T \mathbf{P} \mathbf{B}_{,\beta} (\mathbf{B}^T \mathbf{N}^{-1} \mathbf{B})^{-1} \mathbf{B}^T \mathbf{N}^{-1} + (\mathbf{B}_{,\beta}^T \mathbf{N}^{-1} \mathbf{B} + \mathbf{B}^T \mathbf{N}^{-1} \mathbf{B}_{,\beta}) (\mathbf{B}^T \mathbf{N}^{-1} \mathbf{B})^{-1} \mathbf{B}_{,\beta'}^T \mathbf{P} \right. \right. \\ &\quad \left. \left. + (\mathbf{B}_{,\beta'}^T \mathbf{N}^{-1} \mathbf{B} + \mathbf{B}^T \mathbf{N}^{-1} \mathbf{B}_{,\beta'}) (\mathbf{B}^T \mathbf{N}^{-1} \mathbf{B})^{-1} \mathbf{B}_{,\beta}^T \mathbf{P} - \mathbf{B}_{,\beta}^T \mathbf{N}^{-1} \mathbf{B} (\mathbf{B}^T \mathbf{N}^{-1} \mathbf{B})^{-1} \mathbf{B}^T \mathbf{N}^{-1} \mathbf{B}_{,\beta'} (\mathbf{B}^T \mathbf{N}^{-1} \mathbf{B})^{-1} \mathbf{B}^T \mathbf{N}^{-1} \right. \right. \\ &\quad \left. \left. - \mathbf{B}_{,\beta'}^T \mathbf{N}^{-1} \mathbf{B} (\mathbf{B}^T \mathbf{N}^{-1} \mathbf{B})^{-1} \mathbf{B}^T \mathbf{N}^{-1} \mathbf{B}_{,\beta} (\mathbf{B}^T \mathbf{N}^{-1} \mathbf{B})^{-1} \mathbf{B}^T \mathbf{N}^{-1} \right) \mathbf{D} \mathbf{N}^{-1} \mathbf{B} \right. \\ &\quad \left. \left( \mathbf{B}^T \mathbf{N}^{-1} \mathbf{B}_{,\beta} (\mathbf{B}^T \mathbf{N}^{-1} \mathbf{B})^{-1} \mathbf{B}^T \mathbf{N}^{-1} - \mathbf{B}_{,\beta}^T \mathbf{P} \right) \mathbf{D} \left( \mathbf{N}^{-1} \mathbf{B} (\mathbf{B}^T \mathbf{N}^{-1} \mathbf{B})^{-1} \mathbf{B}_{,\beta'}^T \mathbf{N}^{-1} \mathbf{B} - \mathbf{P} \mathbf{B}_{,\beta'} \right) \right] (\mathbf{B}^T \mathbf{N}^{-1} \mathbf{B})^{-1} \mathbf{E} \quad (\text{A6}) \end{aligned}$$